

Search for Dark Matter in association with a Higgs boson at the LHC: A model independent study

Sweta Baradia^{*1,2}, Sanchari Bhattacharyya^{†3}, Anindya Datta^{‡4}, Suchandra Dutta^{§1,2},
Suvankar Roy Chowdhury^{¶5}, and Subir Sarkar^{||1,2}

¹*Saha Institute of Nuclear Physics, 1/AF Bidhan Nagar, Kolkata, 700064, India*

²*Homi Bhabha National Institute, Training School Complex, Anushaktinagar, Mumbai, 400094, India*

³*Centre for High Energy Physics, Indian Institute of Science, Bengaluru, 560012, India*

⁴*Department of Physics, University of Calcutta, Kolkata, 700009, India*

⁵*University of Petroleum and Energy Studies, Bidholi Via-Prem Nagar, Dehradun, 248007, India*

Abstract

Astrophysical and cosmological observations strongly suggest the existence of Dark Matter. However, its fundamental nature is still elusive. Collider experiments at Large Hadron Collider (LHC) offer a promising way to reveal the particle nature of the dark matter. In such an endeavour, we investigate the potential of the mono-Higgs plus missing E_T signature at the LHC to search for dark matter. Without going in a particular Ultra-Violet complete model of dark matter, we have used the framework of Effective Field Theory to describe the dynamics of a relatively light fermionic dark matter candidate, which interacts with the Standard Model via dimension-6 and dimension-7 operators involving the Higgs and the gauge bosons. Both cut-based and Boosted Decision Tree (BDT) algorithms have been used to extract the signal for dark matter production over the Standard Model backgrounds, assuming an integrated luminosity of 3000 fb^{-1} at $\sqrt{s} = 14 \text{ TeV}$ at the High Luminosity phase of the LHC (HL-LHC). The BDT is seen to separate the dark matter signal at 5σ significance, for masses below 200 GeV , showcasing the prospects of this search at the HL-LHC.

1 Introduction

In the present epoch of precision cosmology, accumulating experimental data from several independent experiments lead us to think about the existence of a new form of matter, namely the Dark Matter (DM), which cannot be accommodated in the paradigm of the Standard Model (SM). Experimental data from the PLANCK satellite [1] conclusively reveal that DM constitutes about 25% of the energy density of the Universe. The surprising fact that the fraction of DM present is overwhelmingly large compared to the luminous matter has also been supported from the analysis of CMBR anisotropy from WMAP [2].

*swetabaradia13@gmail.com

†sanchari1192@gmail.com

‡adphys@caluniv.ac.in

§suchandra.dutta@cern.ch

¶sroychow@cern.ch

||subir.sarkar@cern.ch

More and more indirect evidences in support of the presence of a non-luminous matter in the Universe have been gathered by other satellite based experiments like PAMELA [3], FermiLAT [4], and AMS [5]. In all such experiments, gravitation plays the role of messenger between the DM and standard matter. Thus apart from the fact that the DM interacts via gravity, the exact nature of it is still an enigma.

Unveiling the nature of DM remains a challenge for the particle physics community, as the SM lacks a viable candidate despite strong belief in its particle nature. Initially, neutrinos were thought to play the role of the relic particle. However, relativistic nature of the neutrinos made them unfit for structure formation of the Universe. Consequently, one has to look beyond the SM (BSM) for possible solution of the DM problem. Particle Physics models with Supersymmetry [6,7] and extra dimensions [8] have been theoretically very attractive as both of these large class of models can provide a viable DM candidate apart from offering remedies to many other shortcomings of the SM. Apart from SUSY, Little Higgs model [9], Left-Right Symmetric Models [10,11], models with extended scalar sector [12], or an $U(1)$ extended SM [13] have also been under scrutiny of both the theorists and experimentalists. These theoretical models have been extensively studied and their possible signatures have been looked for at the LHC. Unfortunately, non-observation of any signature at the LHC pertaining to such models only pushes the limits on the masses of such particles to TeV and higher [14].

A couple of conclusions could be drawn from the aforementioned observations. The DM has an origin which is completely decoupled from the SM, and it can only interact via gravitational interactions. On the other hand, a more interesting complete scenario could be such that the SM is a part of it, while the other degrees of freedom are much heavier and beyond the reach of the LHC. The DM is also a part of this model and its interactions to the SM sector are mediated by one or more of such heavy fields. Like many particle physics models of DM [15–17], we will also assume that the relic particle is void of any SM charge, and it interacts with the SM sector via heavy BSM fields. Without going into intricacies of an Ultra-Violet (UV) complete model, the most natural framework to describe such interactions is to construct *effective operators* of dimension higher than four, involving the relic particle with other SM particles respecting all the symmetries of the SM. Such an approach is not very uncommon. Authors in [18,19] have reviewed such possible operators for several variants of relic particle. The particle sector has been extended minimally paving the way for several variants of interactions involving relic and the SM particles. In the present article, we are particularly interested in a scenario with a fermionic relic that interacts with the SM via higher dimensional operators involving the Higgs boson. This approach is same as the effective field theory way to parameterize NP. Several authors have used this approach to propose and study possible signatures of DM. For example, in [20–22], dimension-6 (dim-6) and dimension-7 (dim-7) operators were constructed out of SM fields and a Dirac fermion posing as the relic. Authors in [20] have studied mono-Higgs plus Missing Transverse Energy (MET) final state in pp collision at the LHC as the probe of relic particle production. In a more recent analysis [23], higher dimensional operators involving relic (scalar and fermion) with leptons and gauge bosons have been considered. Final states comprising of a photon or Z -boson have been considered in the future e^+e^- collider. However, none of these analyses have paid any attention to how the unknown coefficient of the operators fare with the measured value of the relic density, or the experimental upper limit on the direct detection cross-section of scattering of relic particles on nucleus.

Previously many authors [13,24–26] have studied the possibility of a DM which has spin- $\frac{1}{2}$, both Dirac and Majorana in nature, with their masses varying from sub-MeV scale to TeV scale. But all such studies involve a plethora of other BSM fields, possibly having masses beyond the reach of the LHC. Looking for a DM signal in such a model dependent framework also requires a careful consideration of the limits on masses and couplings of such heavy fields with the SM particles. It is important to ensure that the effective coupling(s) between the relic and the SM sector result in a relic density and direct detection cross-section in the right ballpark.

So, our aim is two-fold. First, we would like to see what range of values of these effective couplings corresponds to the correct range of values for relic density as well as satisfy the direct detection cross-

section of DM on standard matter. Next, using such values of the effective couplings, we would like to investigate the prospect of exploring signatures of DM due to such interactions at the LHC.

Before we delve into the details of the framework and the analysis, let us emphasise very briefly, the novelties of our analysis.

- We have considered the effect of relic density measurement as well as the upper limit on the cross-section of direct detection on the Wilson coefficients of the dim-6 and dim-7 operators that are defined below.
- The allowed values (from relic density and direct detection measurement) of the Wilson coefficients have been used to estimate the signal strength of mono-Higgs plus MET signal at the LHC.
- We have added the effect of pileup events for all the processes in order to simulate the overlap of multiple pp interactions in the same event, as expected in the HL-LHC conditions. This makes the analysis more realistic.
- In the collider analysis, a cut-based as well as machine learning based algorithm have been used to estimate the signal significance.

The paper is organized as the following. Section 2 covers the description of the framework on which our DM candidate is based, followed by a discussion on all the constraints and other dark matter aspects. In Section 3, the signal and the considered SM background processes are described. Section 3.1 consists of the event selection and analysis strategy followed by cut-based and machine learning based analysis in Section 3.2. Finally, we conclude and summarise our findings in Section 4.

2 Description of Model and Related Dark Matter Aspects

The present framework is model independent consisting of the SM augmented only by a Dirac fermion, playing the role of the relic. Such a particle spectrum at the TeV scale possibly evolves from a UV complete framework with a larger symmetry group, and more particles non-trivially transforming under such symmetry. Such assumption modifies the SM Lagrangian with new effective interactions which are suppressed by heavy mass scale where we believe the New Physics (NP) lies. However, we will not pay much attention to such details but focus ourselves on how these higher dimensional operators may explain the experimental data of relic density and direct detection cross-sections of relic nucleon scattering.

This analysis has been done in the context of DM search in mono-Higgs channel, where the DM candidate, χ is a Dirac-like fermion. The DM candidate, being a SM singlet, does not interact with any SM particles. At this point, we add new interaction terms among DM candidate and SM particles in the form of one dim-6 and two dim-7 effective operators. The effective interactions involving χ , SM Higgs doublet field Φ , $SU(2)_L$ and $U(1)_Y$ gauge field strengths $W_a^{\mu\nu}$, $B^{\mu\nu}$, are given below,

$$\mathcal{O}_1 = \frac{C_1}{\Lambda^2} (\bar{\chi} \gamma_\mu (1 \pm \gamma^5) \chi) (\Phi^\dagger \overleftrightarrow{D}^\mu \Phi) \quad (1)$$

$$\mathcal{O}_2 = \frac{C_2}{\Lambda^3} (\bar{\chi} \sigma_{\mu\nu} \chi) B^{\mu\nu} (\Phi^\dagger \Phi) \quad (2)$$

$$\mathcal{O}_3 = \frac{C_3}{\Lambda^3} (\bar{\chi} \sigma_{\mu\nu} \chi) W_a^{\mu\nu} (\Phi^\dagger \tau_a \Phi) \quad (3)$$

where, Λ is the scale of NP. It is expected that the operators \mathcal{O}_2 and \mathcal{O}_3 can evolve from the same UV complete theory. These two operators generate similar kind of interactions with similar kinematic characteristics in the final state. In the following analysis, we shall be using both the operators simultaneously with equal Wilson coefficients ($C_2 = C_3$). This assumption will simplify our analysis without any

loss of generality. So, from now on, throughout our study we shall consider our new effective Operator 2 as,

$$\mathcal{O}_2 = \frac{C_2}{\Lambda^3} \bar{\chi} \sigma_{\mu\nu} \chi \left[B^{\mu\nu} \left(\Phi^\dagger \Phi \right) + W_a^{\mu\nu} \left(\Phi^\dagger \tau_a \Phi \right) \right] \quad (4)$$

Before going into more rigorous study of production and detection of the DM candidates, let us discuss some details on the DM aspects of this theory in the next section.

2.1 Parameter Constraints from Dark Matter Analysis

The measurement by PLANCK collaboration [1] restricts the density of such invisible matter in a band with its (Ωh^2) central value at 0.12 with a spread of ± 0.001 . This measurement has far reaching consequences not only on the several cosmological scenarios but also on the frameworks beyond the standard model of Particle Physics. A number of theoretical suggestions have been made to explain the measured relic density assuming particle nature of DM, and many of these ideas also have been tested at the LHC. In the present analysis, a Dirac-like fermion Dark Matter candidate, χ , which acts like a Weakly Interacting Massive Particle (WIMP), is being considered. There are three experimental avenues for DM search. In the, *direct detection* experiments signatures for scattering of DM with normal matter is looked for. While in collider experiments one looks for the production signature of DM from the normal matter.

The direct detection experiments like XENON [27, 28], PICO [29], LUX [30] have set an upper limit on DM-nucleon scattering cross-section from the non-observation of any such scattering events. On the other hand, the PLANCK satellite based experiment has measured the relic abundance of our Universe at the present epoch analysing the measured anisotropy of the CMBR spectra. For a convincing particle physics framework for the DM, the model parameters must satisfy the aforementioned constraints. In the following section, we shall present and compare the predictions for direct detection cross-section and relic density in our frameworks with the available experimental data which enables us to have an allowed range of values of the unknown coefficients of the higher dimensional operators defined above. Before we present our results, it should be mentioned that there is a third class of satellite based experiments like PAMELA [3], FermiLAT [4] and AMS [5] which tries to detect the signal of annihilation of DM particles into SM particles. Such experimental data are also available but we have not considered those in our analysis.

2.1.1 Direct Detection and Relic Density

The relic particle χ can scatter elastically over nucleons (see Fig.1), mediated by a Z -boson. With the interactions arising from the \mathcal{O}_1 , χ cannot scatter over nucleons. However, \mathcal{O}_2 can mediate a DM-nucleon scattering. For an estimation of the scattering cross-section, the relevant interactions have been implemented in FeynRules [31], and micrOMEGAs6.0.5 [32] has been used to study the DM aspects of χ .

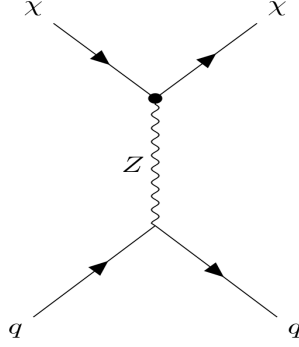


Figure 1: Feynman diagram representing the interactions responsible for direct detection of χ .

Scattering of χ over the nucleons can be both Spin-Independent (SI) and Spin-Dependent (SD). The expressions of Spin-Independent (SI) and Spin-Dependent (SD) scattering cross-sections mediated by a vector boson can be written as [33] the following,

$$(\sigma_{SI})_V \simeq \frac{g_{\chi V}^2 \mu_{\chi N}^2}{\pi M_Z^4} \left[\tilde{f}_p Z + \tilde{f}_n (A - Z) \right]^2 \quad (5)$$

$$(\sigma_{SD})_V \simeq \frac{4g_{\chi A}^2 \mu_{\chi N}^2}{\pi M_Z^4} J_N (J_N + 1) \left[\frac{\langle S_p \rangle}{J_N} \tilde{a}_p + \frac{\langle S_n \rangle}{J_N} \tilde{a}_n \right]^2 \quad (6)$$

where, $\tilde{f}_{p,n}$ and $\tilde{a}_{p,n}$ are dimensionless quantities, which are related to the couplings of the quarks with the mediator. M_Z is the mass of mediating SM Z -boson. $\mu_{\chi N}$ denotes the reduced mass of the WIMP-nucleus system. J_N and $\langle S_{p,n} \rangle$ stand for the spin of the nucleus and the average spin of the nucleons respectively [33].

However, the Spin-Dependent (SD) DM-nucleon scattering cross-section arising due to the interactions present in \mathcal{O}_2 is very small ($\sim 10^{-14}$ pb) compared to the present upper limit provided by PICO Collaboration, whereas for the Spin-Independent (SI) case, masses below 44 (62) GeV are excluded from XENON1T (XENONnT) data for all the values of C_2/Λ^3 considered in our analysis. The SI and SD cross-section are presented in Fig. 2 for a range of values of m_χ and C_2/Λ^3 . The left (right) plot (colored dots) represents the variation of Spin-Independent (Dependent) DM-nucleon scattering cross-section with mass of DM. The color gradient shows the values of C_2/Λ^3 in TeV^{-3} . The solid line in each panel represents the upper limit on the corresponding cross-sections from XENON and PICO experiments at 90% C.L. The Benchmark Points (BP) used in our analysis (defined in the next section) satisfy the direct detection constraints.

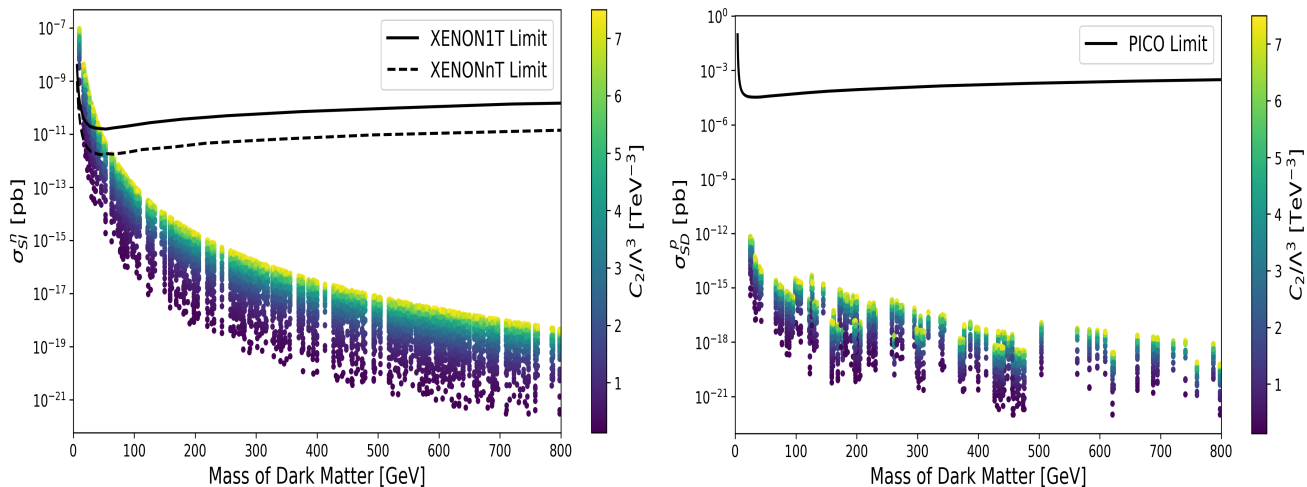


Figure 2: Mass of Dark Matter vs. DM-nucleon scattering cross-section for Signal 2 considering SI (left) and SD (right) case. σ^p and σ^n denote WIMP-proton and WIMP-nucleon scattering cross-sections respectively. The color bar represents the values of C_2/Λ^3 in TeV^{-3} for both plots. The black lines denote the limits from corresponding experiments.

Both the operators \mathcal{O}_1 and \mathcal{O}_2 significantly contribute to the relic abundance of the present Universe. In the early Universe, when the temperature was too high ($T \gg M_\chi$), the SM particles were in thermal equilibrium with the DM particles. The rate of creation and annihilation of Dark Matter were similar. As the Universe gradually cooled down, at $T < M_\chi$, the creation of DM particles from SM particles was forbidden, but the DM-DM annihilation was not. At this point, χ got decoupled from the thermal bath. At the time of freeze-out, the rate of annihilation became equal to the Hubble expansion rate and the remnant amount of DM at that time is the relic density of the Universe. One can estimate this number density solving the Boltzmann equation [34]. In the following, we will study the relic density measurement considering the interactions described by \mathcal{O}_1 and \mathcal{O}_2 .

Solving the Boltzmann equation one can approximately have [35],

$$\Omega h^2 \simeq \frac{0.1 \text{ pb}}{\langle \sigma v \rangle_{eff}} \quad (7)$$

where, h is the Hubble constant and $\langle \sigma v \rangle_{eff}$ is the thermally averaged effective annihilation cross-section times relative velocity of the DM candidate. This expression clearly shows that the larger the annihilation cross-section is, the lower the relic density. In this scenario the DM candidate can annihilate to a pair of SM particles, for example, ZZ , W^+W^- , Zh , $f\bar{f}$ via the effective operators where f is any SM fermion. The Fig. 3 represents the mass of Dark Matter (M_{DM}) vs relic density plot for \mathcal{O}_1 (left) and \mathcal{O}_2 (right), where the color gradient is for the values of the corresponding Wilson coefficients. Here the black band denotes the region where the relic abundance is within PLANCK allowed range i.e., $\Omega h^2 = 0.12 \pm 0.001$ [1]. While considering \mathcal{O}_2 , a pair of relic particles can dominantly annihilate to a pair of SM fermions or W^+W^- via Z boson as a mediator. So when M_{DM} approaches to $M_Z/2$, the annihilation cross-section is very large resulting into very small relic density. This explains the dip near $M_{DM} \simeq M_Z/2$ in the right plot in Fig. 3. On the other hand, for larger values of the Wilson coefficients, the annihilation cross-section increases, hence the relic density decreases. This explains the color gradient of the plots. The benchmark points of our analysis also satisfies the PLANCK limit of the current relic abundance of the Universe.

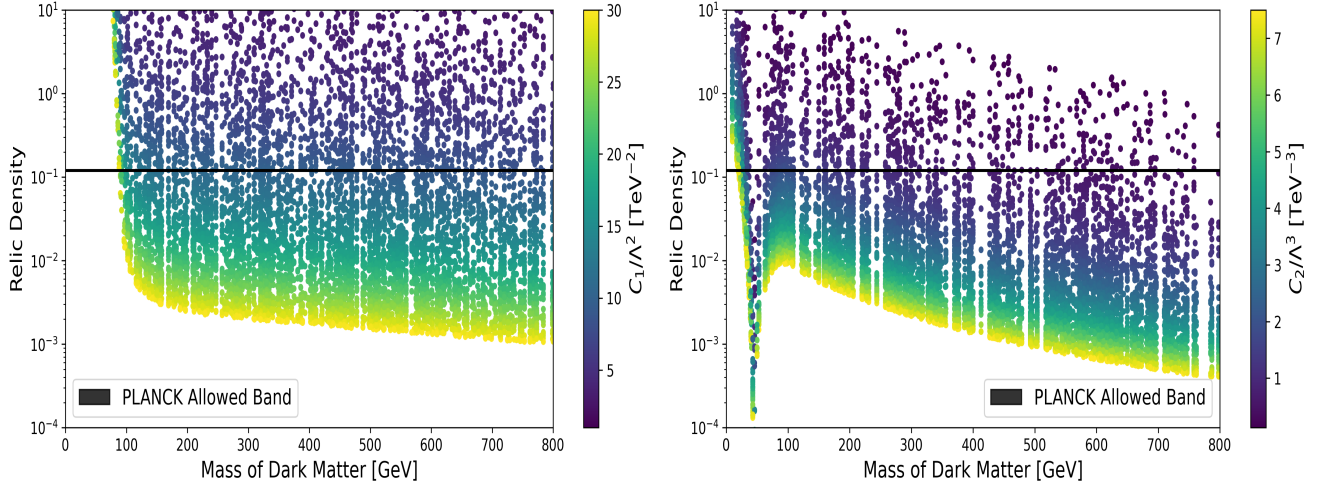


Figure 3: Variation of relic density with dark matter mass for Signal 1 (left) and Signal 2 (right). The color bar represents the values of C_1/Λ^2 in TeV^{-2} (left) and C_2/Λ^3 in TeV^{-3} (right). The black band shows the PLANCK allowed value of the relic density.

3 Collider Search for Dark Matter

In general, production of the relic particle at the LHC will result in missing transverse energy (momentum). For a conclusive signature of χ production one must tag on some objects which could be easily identified at the detector. In view of the effective interactions (Eqs. 1 and 4), the relic particle, χ , can be pair produced along with the SM Higgs boson in quark anti-quark fusion as shown in the Feynman diagrams in Fig. 4. The signal events consist of two b-jets coming from the Higgs boson decay along with a large missing transverse energy (MET). SM processes having similar final states, will act as the background. Hadronic, leptonic and semileptonic decays of $t\bar{t}$, ZZ and Zh processes are the major backgrounds for this analysis.

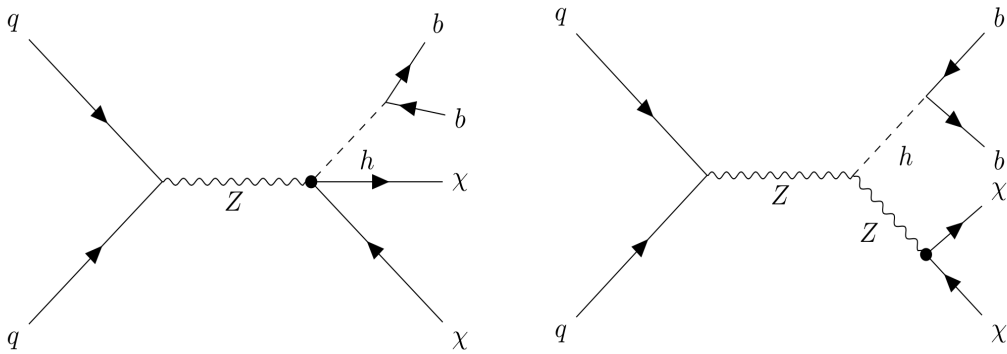


Figure 4: Feynman diagrams describing the effective interactions mentioned in Eqs. 1 and 4.

The signal events have been generated by interfacing `FeynRules` output with the event generator, `MadGraph5_aMC@NLO` [36], requiring a minimum transverse momentum (p_T) of 5 GeV for the b quark. The SM backgrounds are also simulated using `MadGraph5_aMC@NLO` having the same cut on p_T of b quark. For both signal and background samples, `Pythia8` [37] is used for parton showering and hadronisation,

followed by detector simulation in `Delphes3.5.0` [38]. The input card with CMS detector specifications for HL-LHC has been used. A sample of 10^5 minimum bias events are used for pileup mixing with an average pileup of 200. In this analysis, varying the mass of DM (M_χ), six Benchmark Points (BP) have been considered for both the signals, with $C_1/\Lambda^2 = 7.5 \text{ TeV}^{-2}$ for \mathcal{O}_1 and $C_2/\Lambda^3 = 5 \text{ TeV}^{-3}$ for \mathcal{O}_2 . These values of the Wilson coefficients ($C/\Lambda^{2(3)}$) are consistent with the limits on relic density and direct detection cross-section of relic-nucleon scattering. At this point, it is also worth mentioning that these benchmark points also satisfies the upper limit (4 year and 6 year) on thermally averaged annihilation cross-section times relative velocity provided by FermiLAT in $b\bar{b}$ channel. The relic density and cross section times branching fraction for $h \rightarrow b\bar{b}$ for all the different benchmark points are listed in Table 1. One should also mention that the \mathcal{O}_1 and \mathcal{O}_2 can induce Higgs (Z) invisible decay through $hZ\chi\chi$ interaction for relic masses less than $M_h/2$ ($M_Z/2$). In such a case, the limits of Higgs (Z) invisible decay rate would be applicable on the Wilson coefficients. However, for the benchmark points used in our analysis such a decay of the Higgs (Z) boson is kinematically forbidden.

	M_χ (GeV)	Relic Density		$\sigma_{prod} \times BR$ (fb)	
		\mathcal{O}_1	\mathcal{O}_2	\mathcal{O}_1	\mathcal{O}_2
BP1	90	5.56×10^{-2}	1.97×10^{-2}	3.587	1.862
BP2	100	1.08×10^{-2}	2.00×10^{-2}	3.228	1.822
BP3	150	3.16×10^{-3}	1.21×10^{-2}	1.886	1.615
BP4	200	2.47×10^{-3}	8.56×10^{-3}	1.209	1.414
BP5	250	2.19×10^{-3}	6.27×10^{-3}	0.831	1.226
BP6	300	2.00×10^{-3}	4.75×10^{-3}	0.542	1.059

Table 1: Relic density and cross section times branching fraction for different M_χ hypotheses for \mathcal{O}_1 and \mathcal{O}_2 .

Hadronic, leptonic and semileptonic decays of the $t\bar{t}$ process are the dominant sources of background. Each of these produces a $b\bar{b}$ pair in the final state with additional jets, leptons and/or MET. Hadronic decays of $t\bar{t}$ with the highest branching have the MET signature due to jet energy mis-measurements. The semileptonic and leptonic decays have the MET coming from the undetected neutrino (s). A lepton veto at the event level helps in reducing this background. The other major backgrounds in the analysis are ZZ and Zh processes where one of the Z decays into a pair of neutrinos, while the other Z/h decays to a $b\bar{b}$ pair. ZZ and Zh act as resonant backgrounds for the analysis. The cross-section times branching ratio of the background processes are listed in Table 2.

$SMProcess$	$\sigma_{prod} \times BR$ (pb)
$t\bar{t}$ Hadronic ($t\bar{t}H$)	131.381
$t\bar{t}$ Leptonic ($t\bar{t}L$)	20.453
$t\bar{t}$ SemiLeptonic ($t\bar{t}S$)	52.423
ZZ	0.597
Zh	0.104

Table 2: Cross-sections times branching ratio of the SM background processes.

3.1 Event Selection and Analysis Strategy

All the physics objects used in this analysis are reconstructed from the simulated detector response in `Delphes`. The jets are reconstructed using anti- k_t jet clustering algorithm [39] provided in `FastJet` package [40], with a jet radius parameter 0.4. The medium working point provided by `Delphes` has been used for tagging the b-jets. A veto is applied to remove events having isolated leptons with $p_T > 10$ GeV. Jets passing the Pileup Per Particle Identification (PUPPI) algorithm [41] in `Delphes` with $p_T > 35$ GeV are selected. We first compare kinematic variables which give us desired separation between signal and backgrounds. Distributions of the key kinematic variables in signal (\mathcal{O}_1) and background processes, normalized to unity, are shown in Fig. 5.

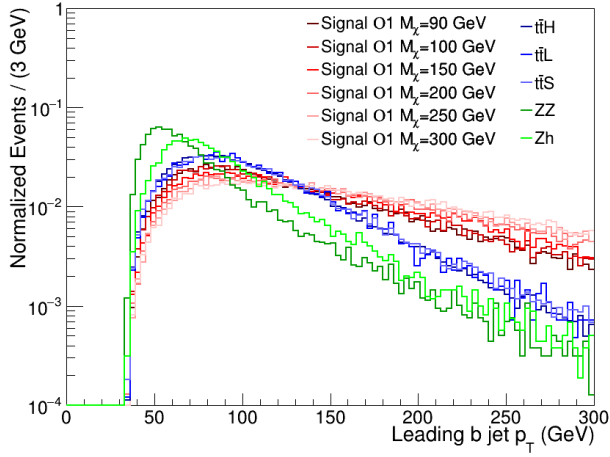
The p_T distribution of the leading and sub-leading b-tagged jets is shown in Figs. 5(a) and 5(b) respectively. The Higgs boson recoils against the DM candidates leading to boosted b-jets in the final state. Fig. 5(c) shows the distribution of MET (\cancel{E}_T). It can be seen that the signal has a large \cancel{E}_T in comparison to background processes, and thus acts as an important variable for discrimination between signal and background. Moreover, the b-jets from signal should have an invariant mass peaking at the mass of the Higgs boson which is visible in Fig. 5(d). The b-jets in Zh process, also coming from the Higgs decay has an invariant mass distribution similar to signal. Figs. 5(e), (f) shows the angular separation, ΔR , between the leading and sub-leading b-jets, and the $\Delta\phi$ between the leading b-jet and \cancel{E}_T , respectively.

We also compare the distributions of MET, leading and sub-leading b-jet p_T , and invariant mass between signal \mathcal{O}_1 and \mathcal{O}_2 as shown in Fig. 6 for $M_\chi = 90$ GeV. All the distributions have been normalized to unity. The p_T and \cancel{E}_T distributions in case of \mathcal{O}_2 are relatively harder than those for \mathcal{O}_1 . This can be accounted by the fact that \mathcal{O}_2 is suppressed by another power of Λ compared to \mathcal{O}_1 . Thus in the former case, cross-section rises more rapidly with energy, resulting into a harder p_T and \cancel{E}_T distributions. Guided by the features observed in the distributions of the key kinematic variables, a cut-based analysis for \mathcal{O}_1 is performed, which is described in the next section.

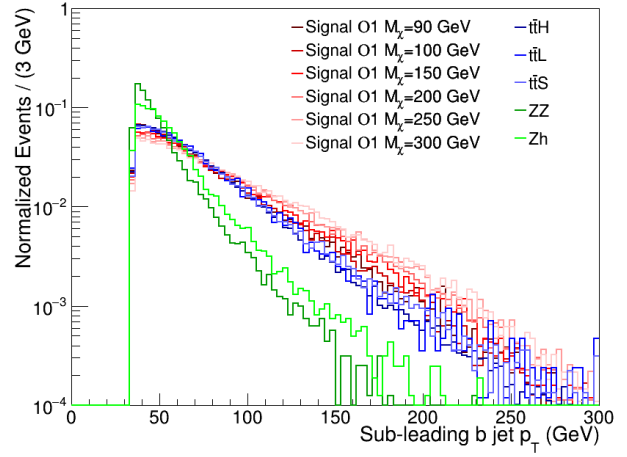
3.2 Analysis

The analysis begins with a pre-selection of events having at least two b-tagged jets and surviving the lepton veto. We first describe the rectangular cut-based analysis, followed by the one using Boosted Decision Tree (BDT) [42]. The sensitivity of the two analysis approaches are demonstrated by computing the signal significance (\mathbf{S}) for all the benchmark points, considering an integrated luminosity (\mathcal{L}) of 3000 fb $^{-1}$ at $\sqrt{s} = 14$ TeV, expected to be delivered by the HL-LHC. The significance is defined as:

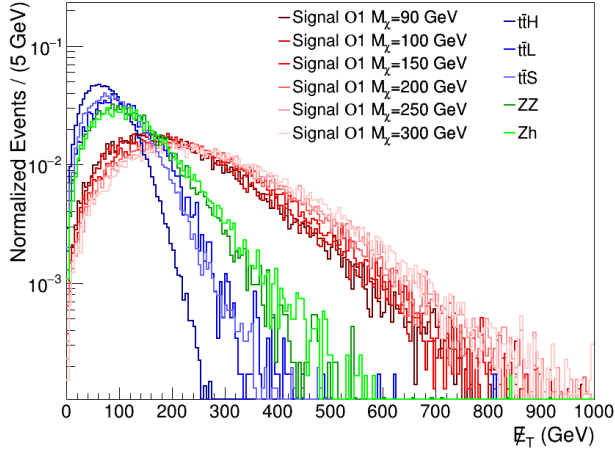
$$\mathbf{S} = \sqrt{2 \left[(S + B) \ln \left(1 + \frac{S}{B} \right) - S \right]} \quad (8)$$



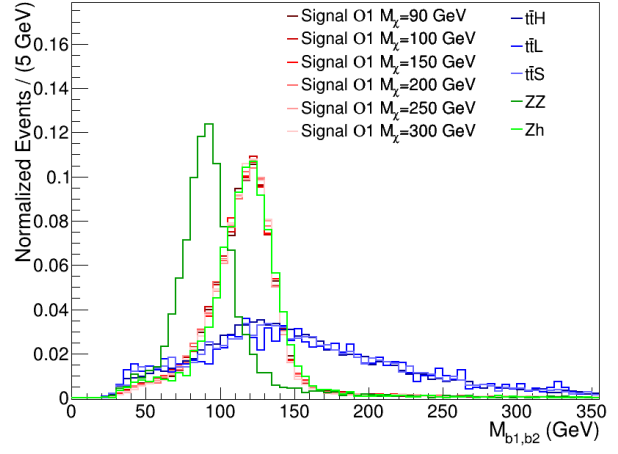
(a) p_T of leading b jet



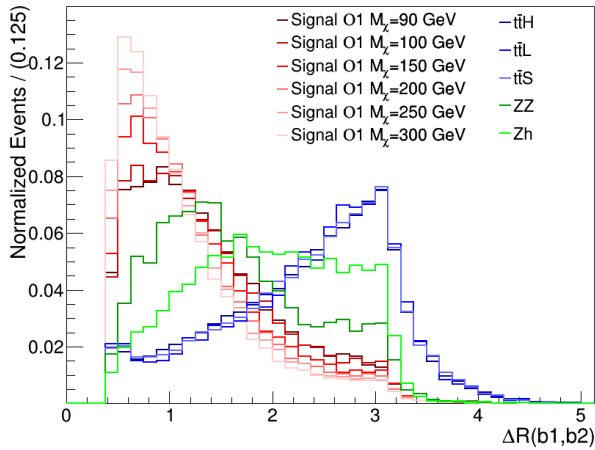
(b) p_T of sub-leading b jet



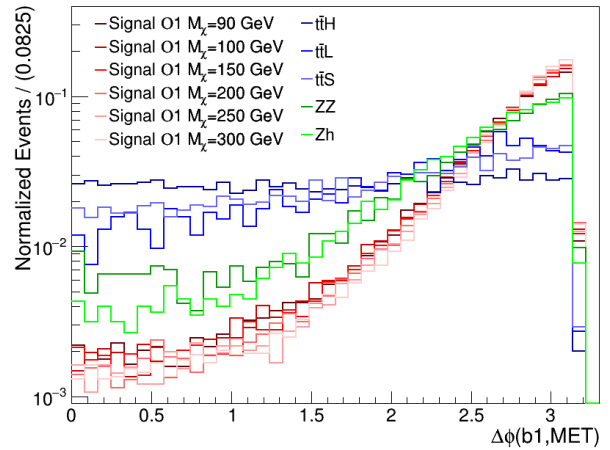
(c) E_T



(d) Invariant mass of the two highest p_T b-jets

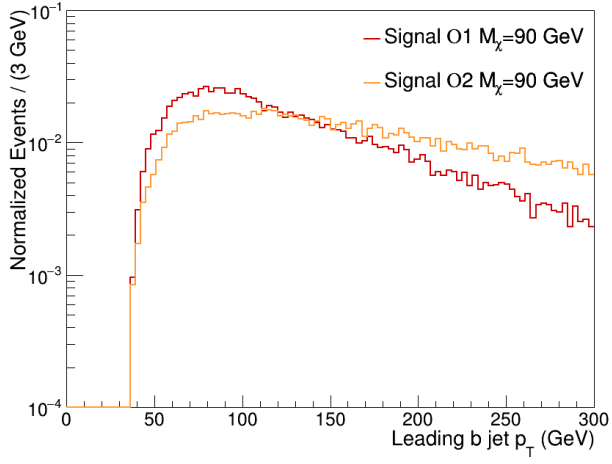


(e) ΔR between the leading and sub-leading b-jets

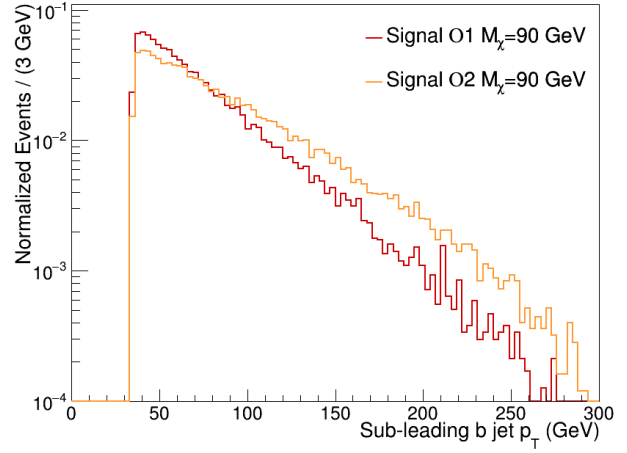


(f) $\Delta\phi$ between the leading b jet and E_T

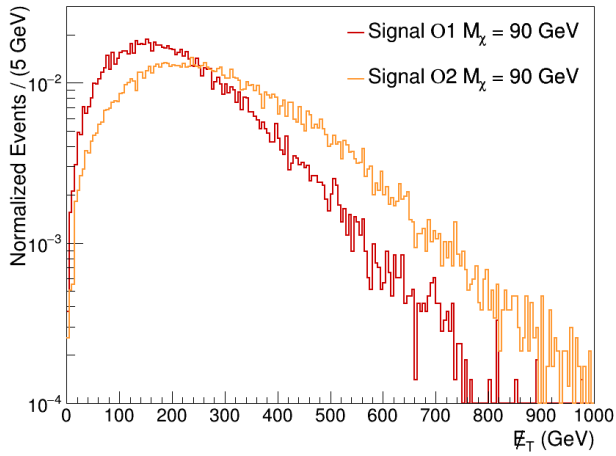
Figure 5: Distributions of key kinematic variables for Signal (\mathcal{O}_1) and background processes, all normalized to unity.



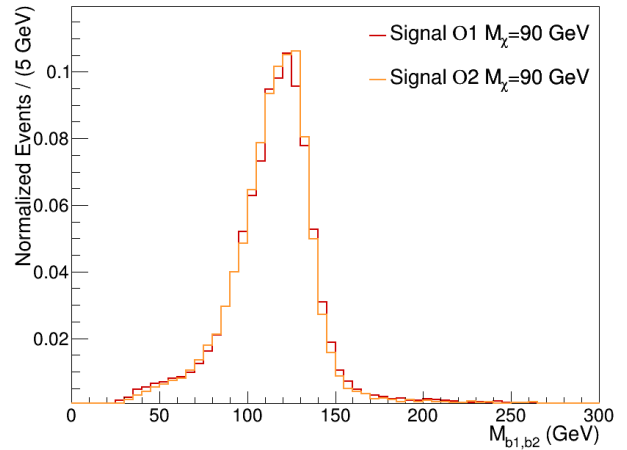
(a) p_T of leading b jet



(b) p_T of sub-leading b jet



(c) \cancel{E}_T



(d) Invariant mass of the two highest p_T b-jets

Figure 6: Distributions of kinematic variables for Signal \mathcal{O}_1 and \mathcal{O}_2 with $M_\chi = 90 \text{ GeV}$, all normalized to unity.

where, S and B are the expected number of signal and background events respectively.

3.2.1 Cut-Based Analysis

The cut-based analysis has been performed for signal \mathcal{O}_1 by applying certain thresholds on the kinematic variables described in Table 3. The selection cuts are applied on events passing the pre-selection mentioned earlier. Table 4 summarizes the cut values along with the signal and background efficiencies.

<i>Variable</i>	<i>Description</i>
$p_{T,b1}$	Transverse momentum of the leading b jet ($b1$)
$\Delta R(b1, b2)$	ΔR between $b1$ and $b2$
\cancel{E}_T	Missing Transverse Energy
$M_{b1,b2}$	Invariant mass of the b jet pair
$p_{T,l1}$	Transverse momentum of the leading non-b jet ($l1$)
$\Delta\phi(b1, \cancel{E}_T)$	$\Delta\phi$ between the $b1$ and \cancel{E}_T
$\Delta\phi(b2, \cancel{E}_T)$	$\Delta\phi$ between $b2$ and \cancel{E}_T

Table 3: List of kinematic variables used in the Cut-Based analysis.

<i>Process</i>	<i>BP1</i>	<i>BP2</i>	<i>BP3</i>	<i>BP4</i>	<i>BP5</i>	<i>BP6</i>	<i>ttH</i>	<i>ttL</i>	<i>ttS</i>	<i>ZZ</i>	<i>Zh</i>
Initial Events	10^5	10^5	10^5	10^5	10^5	10^5	4×10^5	3×10^5	3×10^5	2×10^5	10^5
Cuts											
$p_{T,b1} > 70 \text{ GeV}$	25.7	25.8	27.1	27.9	28.8	28.9	29.4	2.8	7.4	8.0	16.1
$\Delta R(b1, b2) < 1.5$	22.1	22.3	24.3	25.5	26.6	26.9	23.5	2.3	6.1	3.6	10.7
$\cancel{E}_T > 190 \text{ GeV}$	14.9	15.2	17.8	19.6	20.9	21.8	4.2	0.3	1.05	2.1	3.7
$70 \text{ GeV} < M_{b1,b2} < 150 \text{ GeV}$	10.4	10.7	13.3	14.9	16.4	17.3	7.0×10^{-2}	4.0×10^{-2}	0.1	0.6	1.8
$p_{T,l1} < 60 \text{ GeV}$	9.6	9.8	12.2	13.7	15.0	16.1	4.0×10^{-2}	2.0×10^{-2}	6.0×10^{-2}	0.5	1.6
$\Delta\phi(b1, \cancel{E}_T) > 1.5$	6.8	6.9	8.5	9.4	10.2	10.7	1.5×10^{-3}	8.0×10^{-3}	9.0×10^{-3}	0.4	1.2
$\Delta\phi(b2, \cancel{E}_T) > 1.5$	6.8	6.9	8.5	9.4	10.2	10.7	1.5×10^{-3}	8.0×10^{-3}	9.0×10^{-3}	0.4	1.2

Table 4: Kinematic cut efficiencies of signal (\mathcal{O}_1) and backgrounds.

The signal significance is estimated using Eq. 8, after all the selection cuts are applied. The obtained values of significance at $\sqrt{s} = 14 \text{ TeV}$ considering $\mathcal{L} = 3000 \text{ fb}^{-1}$ for all the signal benchmark points of \mathcal{O}_1 are listed in Table 5.

<i>BP (Signal \mathcal{O}_1)</i>	<i>BP1</i>	<i>BP2</i>	<i>BP3</i>	<i>BP4</i>	<i>BP5</i>	<i>BP6</i>
$M_\chi \text{ (GeV)}$	90	100	150	200	250	300
\mathcal{S}	3.8σ	3.5σ	2.5σ	1.8σ	1.3σ	0.9σ

Table 5: Signal significance (\mathcal{S}) for cut-based analysis at $\sqrt{s} = 14 \text{ TeV}$ considering $\mathcal{L} = 3000 \text{ fb}^{-1}$ for all the \mathcal{O}_1 signal benchmark points.

The above results show that the analysis indeed has prospects for the HL-LHC and this motivates us to further explore machine learning algorithm to improve sensitivity. In order to fully exploit the signal

region, and enhance the signal sensitivity we used BDT for both \mathcal{O}_1 and \mathcal{O}_2 signals, as described in the next section.

3.2.2 Analysis using Boosted Decision Tree

BDT is a supervised multivariate technique used in classification problems. It optimizes the separation of signal and background through an ensemble of decision trees. We have used the TMVA-Toolkit for Multivariate Data Analysis [43] package for our study. Except for \cancel{E}_T and $p_{T,l1}$, all the kinematic variables used in the cut-based analysis (Table 3) and a number of new variables defined in Table 6, are used to perform the BDT.

<i>Variable</i>	<i>Description</i>
N_{jets}	Total number of jets
$p_{T,b2}$	Transverse momentum of the sub-leading b jet ($b2$)
$\Delta\phi(b1, l1)$	$\Delta\phi$ between $b1$ and leading non-b jet ($l1$)
$\Sigma p_{T,lj}$	Scalar sum of p_T of light jets
$\Sigma \vec{p}_{T,j}$	Vector sum of p_T of all jets
$\cancel{E}_T / \sqrt{\vec{p}_{T,j}}$	\cancel{E}_T significance defined as $\cancel{E}_T / \sqrt{\vec{p}_{T,j}}$

Table 6: List of kinematic variables used in the BDT based analysis, in addition to the ones mentioned in the cut-based analysis.

The following additional selection cuts have been applied on the pre-selected events before passing them through BDT:

- $p_{T,b1} > 60 \text{ GeV}$
- $\Delta R(b1, b2) < 3$
- $\cancel{E}_T > 120 \text{ GeV}$
- $50 \text{ GeV} < M_{b1,b2} < 250 \text{ GeV}$

Fig. 7 shows the normalized distribution of the input variables to BDT for BP1 signal \mathcal{O}_1 (blue-dashed) and all backgrounds (red-shaded) processes.

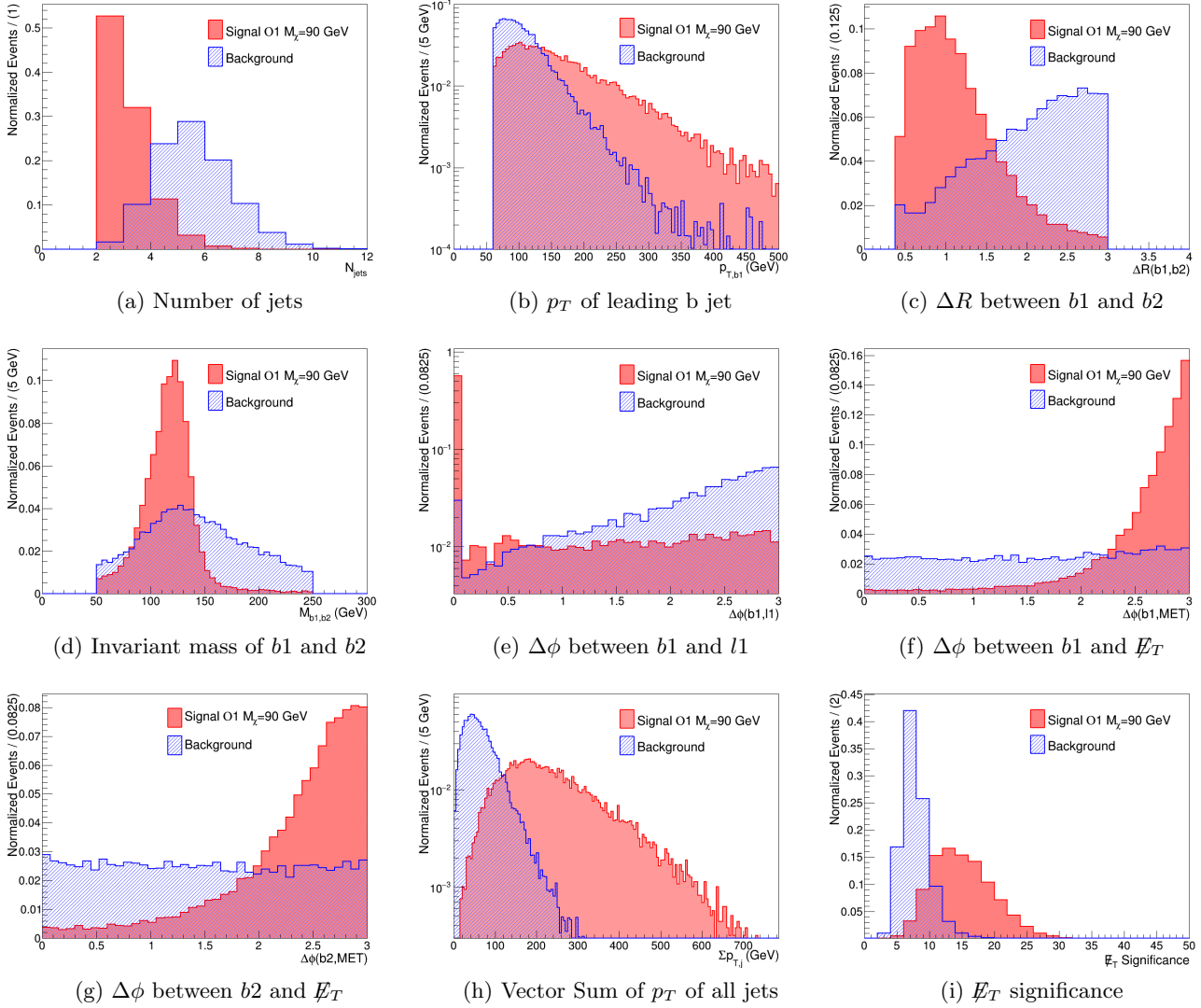


Figure 7: Distributions of feature variables taken as input for BDT in BP1 Signal and Backgrounds

Table 7 shows the values of the BDT parameters used for this analysis. All the benchmark points for both the operators have been trained and tested separately. Sixty percent of the signal and background events are used for training the BDT. The background events are weighted by their cross-sections. The variables are ranked based on how frequently they are used to split nodes in the decision trees. For both the operators, $\Sigma \vec{p}_{T,j}$ and \cancel{E}_T significance are the two most significant variables for signal and background discrimination. The next most important variable is $\Delta\phi(b2, \cancel{E}_T)$ and $M_{b1,b2}$ for \mathcal{O}_1 and \mathcal{O}_2 , respectively.

BDT parameters	Description	Value
NTrees	Number of trees or nodes	850
MinNodeSize	Minimum % of training events required in a leaf node	2.5%
MaxDepth	Max depth of the decision tree allowed	3
BoostType	Boosting mechanism to make the classifier robust	Gradient Boost
Shrinkage	Learning rate for Gradient algorithm	0.5
nCuts	Number of grid points in variable range used in finding optimal cut in node splitting	30

Table 7: List of BDT parameters

We have used the Kolmogorov-Smirnov (KS) test [44] statistic to check that the effect of overtraining is minimal. After successfully running the algorithm we get a well discriminating profile of the BDT response for the signal and backgrounds processes. The distribution of the final BDT response comparing signal, both \mathcal{O}_1 and \mathcal{O}_2 , and total background can be seen in Fig. 8.

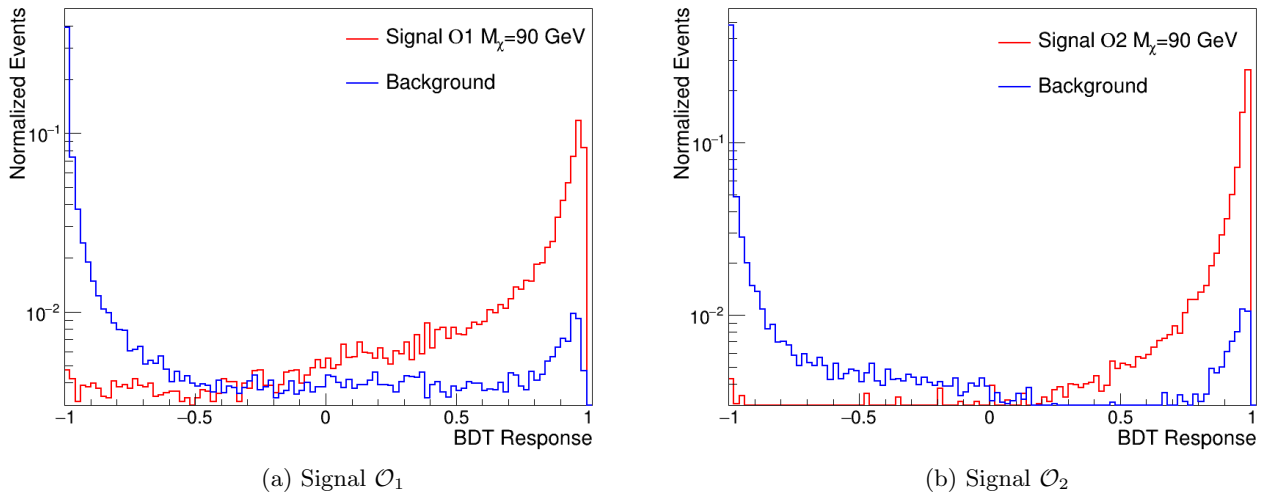


Figure 8: Distribution of BDT response for BP1 Signal, \mathcal{O}_1 and \mathcal{O}_2 , and background, normalized to unity.

Finally, the BDT response is utilized to optimize the signal significance that are recalculated using Eq. 8. The obtained values are listed in Table 8.

M_χ (GeV)	\mathcal{S} Signal \mathcal{O}_1	\mathcal{S} Signal \mathcal{O}_2
90	6.6 σ	5.5 σ
100	6.1 σ	4.9 σ
150	4.4 σ	4.7 σ
200	3.2 σ	4.3 σ
250	2.4 σ	3.5 σ
300	1.7 σ	3.3 σ

Table 8: Signal significance for BDT at $\sqrt{s} = 14$ TeV considering $\mathcal{L} = 3000 \text{ fb}^{-1}$ for all the signal benchmark points.

The signal significance improves notably for all the benchmark points with BDT compared to the cut-based analysis which can be seen in Tables 5 and 8. For BP1 and BP2, we obtain a signal significance of 6.6 σ and 6.1 σ for \mathcal{O}_1 , respectively. The same for \mathcal{O}_2 is 5.5 σ and 4.9 σ .

4 Summary and Conclusion

To summarise, we have considered a model independent approach to investigate the prospect of discovering the relic particle at the high luminosity run of the LHC. The proposed relic particle, a Dirac fermion in our framework, has no charge under SM gauge group. However, its mass is well within the kinematic reach of the HL-LHC. Such a particle can arise in an UV complete BSM theory. Such a model may also consist of a plethora of other particles, which are possibly too heavy, and are beyond the reach of the LHC. An apt way to describe the physics of such a scenario is using the framework of effective field theory, where the fields with masses comparable with energy scale of interest are the only relevant degrees of freedom and the fields which are much heavier are integrated out. Consequently, one is left with certain higher (> 4) dimensional operators which are suppressed by appropriate powers of energy scale and have unknown coefficients. We have exactly followed the same prescription, by constructing dim-6 and dim-7 operators involving the relic particle (χ), Higgs boson and gauge bosons of the SM. These operators could be viewed as the only portal to the dark sector and are responsible for any interaction of relic particle with the SM particles. Consequently, the unknown Wilson coefficients of the proposed operators could be constrained from the measurement of relic density and experimental upper limits on the DM-nucleon scattering cross-section.

To begin with we determined the allowed range of values of the Wilson coefficients by comparing the model predictions for the aforementioned quantities with the experimental data scanned over a range of mass of DM starting from 10 GeV to 800 GeV. Results from XENON excludes DM masses below 62 GeV for dim-7 operator, \mathcal{O}_2 . Next, we set to explore the prospect of producing the relic particles in association with the SM Higgs boson via the higher dimensional interactions at the LHC. The Higgs boson will subsequently decay to a pair of b -quarks resulting in two b -jets plus missing E_T as the final state. Similar final state can arise from various other SM processes like $t\bar{t}$, ZZ and Zh . In order to estimate the SM contribution to such a final state, the contributions from pileup events have also been taken into account. Using simulation samples for signal and SM backgrounds, we have performed both cut-based and BDT based analysis in the HL-LHC scenario. Considering a projected $\mathcal{L} = 3000 \text{ fb}^{-1}$ to be recorded at the HL-LHC, our results show that for \mathcal{O}_1 and \mathcal{O}_2 a signal significance of 6.6 – 1.7 σ and 5.5 – 3.3 σ respectively, can be achieved for a range of DM mass varying from 90 GeV to 300 GeV.

References

- [1] PLANCK collaboration, *Planck 2018 results. VI. Cosmological parameters*, *Astron. Astrophys.* **641** (2020) A6 [[1807.06209](#)].
- [2] C.L. Bennett, D. Larson, J.L. Weiland, N. Jarosik, G. Hinshaw, N. Odegard et al., *Nine-Year Wilkinson Microwave Anisotropy Probe (WMAP) Observations: Final Maps and Results*, *The Astrophysical Journal Supplement Series* **208** (2013) 20.
- [3] C.L.B. et al, *Measurement of the flux of primary cosmic ray antiprotons with energies of 60 MeV to 350 GeV in the PAMELA experiment*, *JTEP* **96** (2013) 621–627.
- [4] THE FERMI-LAT collaboration, *Searching for Dark Matter Annihilation from Milky Way Dwarf Spheroidal Galaxies with Six Years of Fermi Large Area Telescope Data*, *Phys. Rev. Lett.* **115** (2015) 231301.
- [5] S.-J. Lin, X.-J. Bi, P.-F. Yin and Z.-H. Yu, *Implications for dark matter annihilation from the AMS-02 \bar{p}/p ratio*, [1504.07230](#).
- [6] G. Jungman, M. Kamionkowski and K. Griest, *Supersymmetric dark matter*, *Physics Reports* **267** (1996) 195.
- [7] C. Munoz, *Models of Supersymmetry for Dark Matter*, *EPJ Web Conf.* **136** (2017) 01002 [[1701.05259](#)].
- [8] D. Hooper and S. Profumo, *Dark matter and collider phenomenology of universal extra dimensions*, *Physics Reports* **453** (2007) 29.
- [9] A. Freitas, P. Schwaller and D. Wyler, *A Little Higgs Model with Exact Dark Matter Parity*, *JHEP* **12** (2009) 027 [[0906.1816](#)].
- [10] T. Bandyopadhyay and A. Raychaudhuri, *Left–right model with TeV fermionic dark matter and unification*, *Phys. Lett. B* **771** (2017) 206 [[1703.08125](#)].
- [11] S. Bhattacharyya and A. Datta, *Dark matter perspective of left-right symmetric gauge model*, *Nucl. Phys. B* **991** (2023) 116197 [[2206.13105](#)].
- [12] S. Bhattacharya, P. Ghosh, A.K. Saha and A. Sil, *Two component dark matter with inert Higgs doublet: neutrino mass, high scale validity and collider searches*, *JHEP* **03** (2020) 090 [[1905.12583](#)].
- [13] D. Nanda and D. Borah, *Common origin of neutrino mass and dark matter from anomaly cancellation requirements of a $U(1)_{B-L}$ model*, *Phys. Rev. D* **96** (2017) 115014 [[1709.08417](#)].
- [14] CMS collaboration, *Dark sector searches with the CMS experiment*, [2405.13778](#).
- [15] I. Hierro, S. King and S. Rigolin, *Higgs portal dark matter and neutrino mass and mixing with a doubly charged scalar*, *Physics Letters B* **769** (2017) 121.
- [16] M. Chianese, B. Fu and S.F. King, *Dark Matter in the Type Ib Seesaw Model*, *JHEP* **05** (2021) 129 [[2102.07780](#)].
- [17] M. Chianese, B. Fu and S.F. King, *Interplay between neutrino and gravity portals for FIMP dark matter*, *JCAP* **01** (2021) 034 [[2009.01847](#)].

- [18] J.C. Criado, A. Djouadi, M. Perez-Victoria and J. Santiago, *A complete effective field theory for dark matter*, *JHEP* **07** (2021) 081 [2104.14443].
- [19] J.-H. Liang, Y. Liao, X.-D. Ma and H.-L. Wang, *Dark sector effective field theory*, *JHEP* **12** (2023) 172 [2309.12166].
- [20] A.A. Petrov and W. Shepherd, *Searching for dark matter at LHC with mono-Higgs production*, *Physics Letters B* **730** (2014) 178.
- [21] A. Berlin, T. Lin and L.-T. Wang, *Mono-Higgs Detection of Dark Matter at the LHC*, *JHEP* **06** (2014) 078 [1402.7074].
- [22] K. Ghorbani and L. Khalkhali, *Mono-Higgs signature in a fermionic dark matter model*, *J. Phys. G* **44** (2017) 105004 [1608.04559].
- [23] S. Bhattacharya, P. Ghosh, J. Lahiri and B. Mukhopadhyaya, *Mono-X signal and two component dark matter: New distinction criteria*, *Phys. Rev. D* **108** (2023) L111703 [2211.10749].
- [24] E. Bernreuther, S. Heeba and F. Kahlhoefer, *Resonant sub-GeV Dirac dark matter*, *JCAP* **03** (2021) 040 [2010.14522].
- [25] A. Carmona, J. Castellano Ruiz and M. Neubert, *A warped scalar portal to fermionic dark matter*, *Eur. Phys. J. C* **81** (2021) 58 [2011.09492].
- [26] R. Cepedello, F. Esser, M. Hirsch and V. Sanz, *SMEFT goes dark: Dark Matter models for four-fermion operators*, *JHEP* **09** (2023) 081 [2302.03485].
- [27] XENON collaboration, *First Dark Matter Search with Nuclear Recoils from the XENONnT Experiment*, *Phys. Rev. Lett.* **131** (2023) 041003 [2303.14729].
- [28] XENON collaboration, *Dark Matter Search Results from a One Ton-Year Exposure of XENON1T*, *Phys. Rev. Lett.* **121** (2018) 111302 [1805.12562].
- [29] PICO collaboration, *Search for inelastic dark matter-nucleus scattering with the PICO-60 CF3I and C3F8 bubble chambers*, *Phys. Rev. D* **108** (2023) 062003 [2301.08993].
- [30] LUX collaboration, *Limits on spin-dependent WIMP-nucleon cross section obtained from the complete LUX exposure*, *Phys. Rev. Lett.* **118** (2017) 251302 [1705.03380].
- [31] A. Alloul, N.D. Christensen, C. Degrande, C. Duhr and B. Fuks, *FeynRules 2.0 - A complete toolbox for tree-level phenomenology*, *Comput. Phys. Commun.* **185** (2014) 2250 [1310.1921].
- [32] G. Belanger, A. Mjallal and A. Pukhov, *Recasting direct detection limits within micrOMEGAs and implication for non-standard Dark Matter scenarios*, *Eur. Phys. J. C* **81** (2021) 239 [2003.08621].
- [33] A. Berlin, D. Hooper and S.D. McDermott, *Simplified Dark Matter Models for the Galactic Center Gamma-Ray Excess*, *Phys. Rev. D* **89** (2014) 115022 [1404.0022].
- [34] A. Ahmed, M. Duch, B. Grzadkowski and M. Iglicki, *Multi-Component Dark Matter: the vector and fermion case*, *Eur. Phys. J. C* **78** (2018) 905 [1710.01853].
- [35] S. Bhattacharya, P. Poulose and P. Ghosh, *Multipartite Interacting Scalar Dark Matter in the light of updated LUX data*, *JCAP* **04** (2017) 043 [1607.08461].

- [36] J. Alwall, R. Frederix, S. Frixione, V. Hirschi, F. Maltoni, O. Mattelaer et al., *The automated computation of tree-level and next-to-leading order differential cross sections, and their matching to parton shower simulations*, *Journal of High Energy Physics* **2014** (2014) .
- [37] C. Bierlich, S. Chakraborty, N. Desai, L. Gellersen, I. Helenius, P. Ilten et al., *A comprehensive guide to the physics and usage of PYTHIA 8.3*, 2022.
- [38] J. de Favereau, C. Delaere, P. Demin, A. Giammanco, V. Lemaître, A. Mertens et al., *DELPHES 3: a modular framework for fast simulation of a generic collider experiment*, *Journal of High Energy Physics* **2014** (2014) .
- [39] M. Cacciari, G.P. Salam and G. Soyez, *The anti-ktjet clustering algorithm*, *Journal of High Energy Physics* **2008** (2008) 063–063.
- [40] M. Cacciari, G.P. Salam and G. Soyez, *FastJet user manual: (for version 3.0.2)*, *The European Physical Journal C* **72** (2012) .
- [41] B. Kreis, *Particle Flow and PUPPI in the Level-1 Trigger at CMS for the HL-LHC*, 2018.
- [42] Y. Coadou, *Boosted Decision Trees*, in *Artificial Intelligence for High Energy Physics*, p. 9–58, WORLD SCIENTIFIC (2022), DOI.
- [43] A.H. et al., *TMVA - Toolkit for Multivariate Data Analysis*, 2009. physics/0703039.
- [44] R. Lopes, *Kolmogorov-Smirnov Test*, pp. 718–720 (2011), DOI.